Late Triassic extensional tectonics in the northern North China Craton, insights from a multidisciplinary study of the Wangtufang pluton

Huabiao Qiu, Wei Lin, Michel Faure, Yan Chen, Lingtong Meng, Jipei Zeng, Zhiheng Ren, Yin Wang, Qiuli Li

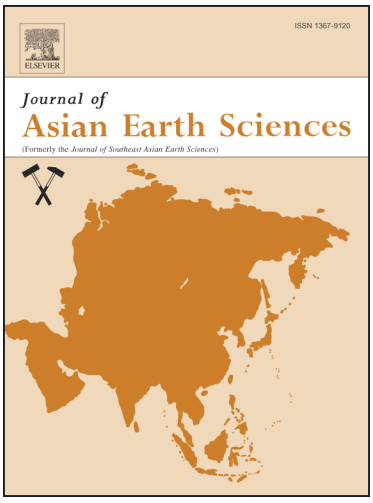

Late Triassic extensional tectonics in the northern North China Craton, insights from a multidisciplinary study of the Wangtufang pluton

Huabiao Qiu, Wei Lin, Michel Faure, Yan Chen, Lingtong Meng, Jipei Zeng, Zhiheng Ren, Yin Wang, Qiuli Li

PII: S1367-9120(20)30255-8
DOI: https://doi.org/10.1016/j.jseaes.2020.104462
Reference: JAES 104462

To appear in: *Journal of Asian Earth Sciences*

Received Date: 20 March 2020
Revised Date: 7 June 2020
Accepted Date: 7 June 2020

Please cite this article as: Qiu, H., Lin, W., Faure, M., Chen, Y., Meng, L., Zeng, J., Ren, Z., Wang, Y., Li, Q., Late Triassic extensional tectonics in the northern North China Craton, insights from a multidisciplinary study of the Wangtufang pluton, *Journal of Asian Earth Sciences* (2020), doi: https://doi.org/10.1016/j.jseaes.2020.104462

Late Triassic extensional tectonics in the northern North China Craton, insights from a multidisciplinary study of the Wangtufang pluton

Huabiao Qiu[1,2,3], Wei Lin[1,3*], Michel Faure[2], Yan Chen[2], Lingtong Meng[1,3], Jipei Zeng[1,3], Zhiheng Ren[1,3], Yin Wang [1,3], and Qiuli Li[1]

[1]State Key Laboratory of Lithospheric Evolution, Institute of Geology and Geophysics, Innovation Academy for Earth Science, Chinese Academy of Sciences, Beijing100029, China

[2]Univ. Orléans, CNRS, BRGM, ISTO, UMR 7327, F-45071, Orléans, France

[3]University of Chinese Academy of Sciences, Beijing100049, China

[*]Corresponding author: (linwei@mail.iggcas.ac.cn)

Postal address: No. 19, Beitucheng Western Road, Chaoyang District, 100029, Beijing, P.R.China

Abstract

To better understand Late Triassic tectonic setting in the northern North China Craton (NCC), the emplacement mechanism of the Wangtufang pluton, which recorded the synmagmatic regional tectonic signature, has been investigated. Zircon U-Pb ages, and Hf isotopic data, and whole-rock geochemical analyses suggest that the Late Triassic Wangtufang pluton composed of syenogranite and diorite is derived from partial melting of lower crust with some depleted mantle components. Both the syenogranite and diorite appear isotropic. Anisotropy of magnetic susceptibility and gravity studies have been carried out to characterize internal fabrics and shape of the pluton. The diorite forms just thin remnants above the syenogranite. The syenogranite with a series of NW-SE trending dykes intruded into the diorite and its country rocks. In the syenogranite, the gently dipping magnetic foliations strike nearly parallel to the pluton border. The shallow plunging magnetic lineations mainly strike NE–SW. Combining NE-SW trending elongated subsurface shape with central root, unflat bottom, and moderate- to high- inward dipping sidewalls, the syenogranite could be considered as a lopolith-like intrusion. The syenogranite was likely emplaced by inflation of magma pulses from its central conduit and built up by floor depression. Emplacement of the syenogranite was in an extensional setting, considering: (1) the NE–SW striking magnetic lineation, (2) the NE–SW trending elongated subsurface pluton shape, and (3) the orthogonal NW–SE striking syenogranitic dykes considered as tension gashes during the NE–SW trending extension. The Wangtufang pluton provides reliable arguments to the Late Triassic intracontinental extensional setting already suggested in the northern NCC.

Key words: North China Craton; early Mesozoic magmatism; Wangtufang pluton; multidisciplinary study; Late Triassic extensional tectonics

1. Introduction

The early Mesozoic magmatism, represented by E–W trending Late Triassic alkaline intrusive complexes, is conspicuous in the northern NCC. However, their tectonic and geodynamic settings are still debated (Yang et al., 2012; Zhang et al., 2012; Zhao et al., 2015). Based on structural observations and paleomagnetic studies, one group of researchers considers that these Late Triassic granitic and syenitic plutons were due to large-scale Triassic thrusting and strike-slip faulting in the northern margin of the NCC and produced in the local extensional areas by the pull-apart of the strike-slip faults (e.g., Zhao et al., 2015). According to geochemical studies, another group proposes that the Late Triassic alkaline complexes in the northern NCC, especially silica-undersaturated syenites, occurred in an intracontinental extensional tectonic setting (e.g., Yang et al., 2012; Zhang et al., 2012), implying the early timing of cratonic destruction during the Late Triassic (Han et al., 2004). The Late Triassic tectonic regime is important to understand the tectonic and geodynamic evolution of the NCC. However, only few small remnants of Late Triassic sedimentary basins can be observed and offer little coeval structural information in the northern NCC due to the intense post-Triassic tectonics (i.e., Xiabancheng basin and Niuyingzi-Dengzhangzi basin in the Yanshan Fold-and-Thrust Belt (YFTB); Fig. 1; Davis et al., 2009; Meng et al., 2014). Moreover, it is difficult to recognize the regional tectonic framework from these few small remnant basins. Due to less impressive and controversial evidence, the nature of the Triassic regime is in debate since long time with different hypotheses. Late Triassic contractional tectonics was proposed according to the unconformity between Triassic and Lower Jurassic strata, and Lower Jurassic syntectonic conglomerate (Zhao, 1990; Liu et al., 2012). Detrital zircon dating and sedimentary studies suggest that the conformable Upper Triassic strata were deposited in an extensional setting (Davis et al., 2009; Meng et al., 2014; Meng et al., 2019). Consequently, the paucity of structural data makes difficult to assess the Late Triassic tectonic regime.

During pluton emplacement, magma fabrics can potentially record information on both magma dynamics and regional strain fields to which the magma was subjected (e.g., Bouchez, et al., 1997; Paterson et al., 1998; Sant'Ovaia et al., 2000). The solid-state fabrics present structural deformation after magma full crystallization (Paterson et al., 1989). Therefore, the fabric pattern and shape of pluton are crucial to decipher the pluton emplacement process. The structural study of plutons is an effective and practical way to unravel regional tectonic setting coeval with the emplacement process (e.g., Bouchez, et al., 1997; De Saint Blanquat et al., 2011). Numerous studies have proven that the fabrics of granitic plutons may provide signatures of the local and regional constraints on the pluton emplacement (e.g., Paterson et al., 1998; De Saint Blanquat et al., 2011; Lin et al., 2013b). Therefore, Late Triassic plutons from the NCC present good opportunities to realize this purpose, and, accordingly, the Wangtufang pluton was chosen for this study (Fig. 1). Indeed, such studies have been rarely performed on Late Triassic plutons of the northern NCC. An integrated multidisciplinary investigation, including structural geology, geochronology, geochemistry, Anisotropy of magnetic susceptibility (AMS), and gravity modeling, has been conducted to decipher the Late Triassic tectono-magmatic setting in the northern NCC. Given the correlation with other contemporaneous plutons or tectonics, the proposed model may have regional implications for the Late Triassic tectonic setting in the northern NCC.

2. Geological setting

After its assembly through the collision of the Eastern, Intermediate (or Fuping), and Western blocks during the Paleoproterozoic (Zhao et al., 2001; Faure et al., 2007; Li and Zhao et al., 2007; Li et al., 2012), the NCC formed a stable craton from Mesoproterozoic to Paleozoic. Archaean and Paleoproterozoic gneiss, migmatites and granites were overlain by a

Mesoproterozoic to Permian sedimentary cover, separated by a widespread disconformity between the Middle Ordovician and Upper Carboniferous sequences (Li et al., 2016). The closure time of the Paleo-Asian Ocean to the north of the NCC is still controversial. Some authors argue for a Late Permian to the Early Triassic age (e.g., Windley et al. 2007; Xiao et al., 2015), whereas others propose the Paleo-Asian Ocean closed during the Late Devonian, followed by the Late Carboniferous–Triassic intracontinental tectonics (Xu et al., 2013; Zhao et al., 2013). In the south, the NCC collided with the South China Block before the Middle Devonian (e.g., Mattauer et al., 1985; Xu et al., 1986) or in the Triassic (e.g., Meng and Zhang, 1999; Hacker et al., 2000; Li et al., 2010, 2011, 2017, 2018). In the YFTB, the E-W trending ductile shear zone and thick- and thin-skinned folds and faults occurred progressively from the northern margin toward the interior (Wang et al., 2013). The ductile shear zone concerns the E-W trending Chicheng - Fengning, Fengning - Longhua, and Damiao – Niangniangmiao ductile shear zones in the north (Wang et al., 2013; Zhang et al., 2014; Figure 1), and the E-W trending folds and thrusts include the Unnamed fault, Malanyu anticline, and Jixian thrust fault in the south (Davis et al., 2001; Ma et al., 2007). Few Triassic remnant basins and a large number of contemporaneous plutons are exposed in the northern NCC (Davis et al., 2009; Zhang et al., 2012; Meng et al., 2014).

During the Jurassic to earliest Cretaceous, the Mongol-Okhotsk Ocean closed progressively from west to east in the north of the East Asian continent (Zorin, 1999; Daoudene et al., 2013). Meanwhile, the subduction of the Paleo-Pacific Ocean plate occurred in the southeast of the East Asian continent (Davis et al., 2001). A large scale intra-continental deformation and magmatism, traditionally referred to as the Yanshanian movement, occurred in the NCC (Davis et al., 2001; Faure et al., 2012; Zhang et al., 2014; Dong et al., 2015). The YFTB is a typical intracontinental orogen, formed in the northern part of the NCC (Davis et al., 2001). The thrust

faults, which strike E–W in the west and NE–SW in the east, are distributed throughout the YFTB (e.g., Davis et al., 2001; Faure et al., 2012; Fig. 1). As mentioned above, due to the intense deformation during the Jurassic Yanshanian contractional events, only few pre-Jurassic structures could be surely recognized in the YFTB (e.g., Davis et al., 2009; Zhang et al., 2012; Meng et al., 2014; Zhang et al., 2014; Fig.1). In the Early Cretaceous, the NCC was dominated by extensional tectonics (i.e., metamorphic core complexes (MCCs), A-type magmatism, graben or half-graben basins; Li et al., 2012; Zhang et al., 2014, Lin et al., 2018).

3. Structural observations

3.1 Field observations

The Wangtufang pluton has a subcircular surface exposure with a radius of about 12 km. It mainly consists of syenogranite in the southwest and diorite in the northeast (Fig. 2). Macroscopically, these two types of rocks (i.e., pale red syenogranite and dark gray diorite) appear totally isotropic, lacking of any planar and linear structures at outcrops (Figs. 3a and 3b). The main rock-forming minerals, namely, quartz, K-feldspar, plagioclase, amphibole, and biotite, are generally euhedral to subhedral without obvious preferred orientation. The Wangtufang pluton intrudes into foliated, even mylonitic Archaean gneiss and undeformed migmatitic granite (Lin et al., 2013a; Fig. 2). In the gneiss, in spite of the strike variation of foliation, the mineral and stretching lineations are consistently oriented along a NW–SE direction (Figs. 2 and 3c–3d). A top-to-the SE sense of shear is indicated by sigmoidal K-feldspar porphyroclasts (Fig. 3e). The gneiss is pervasively folded by the top-to-the SE shearing, indicative of strong deformation before pluton emplacement. In the northwest, steep and weak foliations are developed in the migmatitic granite near the contact with the diorite (Figs. 2 and 3f). A remnant of the country rocks is

130 preserved in the southeast of the syenogranite (Fig. 2). The pluton is overlain by Cretaceous
131 pyroclastic rocks in its east (Fig. 2).

132 In the Wangtufang pluton, centimeter to ten-meter wide syenogranitic dykes extensively
133 intrude in the diorite (Fig. 2). Meter-scale dykes intruded into the diorite near the contact between
134 the syenogranite and diorite (Fig. 4a). Locally, diorite blocks are included in syenogranite dykes
135 (Fig. 4b). The contact between syenogranite and drop blocks of diorite is sharp. It can be observed
136 that numerous dykes of the syenogranite intruded into the diorite in its northeasternmost (Fig. 4c).
137 Furthermore, all dykes are steep and strike consistently NW–SE direction (Fig. 2). In the
138 syenogranite, several ten-meter xenoliths in diameter of the diorite are scattered in the syenogranite
139 (Fig. 4d). A remnant of diorite remains in the center of the syenogranite (Fig. 2). These phenomena
140 show that the diorite was dismembered by the intrusion of the syenogranite with a series of dykes
141 after the diorite had fully crystallized.

142 **3.2 Microscopic observations**

143 To determine the relationships between the minerals and magnetic fabrics, microstructures
144 are investigated in 36 sampling sites of the Wangtufang pluton (Fig. 5a). Under the microscope,
145 two textural types can be distinguished in the Wangtufang pluton. At most sites (67%), the
146 Wangtufang pluton presents magmatic fabrics without any evidence of deformation (Figs. 5a–5c).
147 Quartz crystals are anhedral, non-deformed, and do not show signs of undulose extinction or
148 dynamic recrystallization. K-feldspars present Carlsbad twinning and marginal replacement by
149 myrmekite (Fig. 5b). The euhedral biotite flakes have a sharp extinction and are neither kinked nor
150 bent (Fig. 5c). Plagioclase grains are euhedral and exhibit Carlsbad-albite compound twinning and
151 polysynthetic twinning (Fig. 5c). Besides, at some sites (33%), submagmatic fabrics can be also
152 observed (Fig. 5a). Millimeter-sized quartz grains show an undulose extinction, and small well-

individualized quartz grains occur at the border of the coarse grains (Figs. 5d and 5e). Generally, significant solid-state deformation has not been observed. The fabrics are mostly acquired in magmatic state but record some submagmatic deformation.

4. Geochronology and geochemistry

4.1 Zircon U–Pb geochronology

Considering the paucity of available dating in this pluton, new zircon U-Pb dating of two samples WTF5 and WTF13 was performed by a Cameca IMS 1280 large-radius SIMS at the Institute of Geology and Geophysics, Chinese Academy of Sciences (IGGCAS), Beijing (Fig. 2; Tab. 1). The zircon grains from these two samples are subhedral, transparent, and 50–150 μm in length with aspect ratios between 1:1 and 3:1. CL images show clear oscillatory zoning (Fig. 6). Th/U ratios of Sample WTF5 vary from 0.42 to 1.12. Twenty analyses of $^{206}Pb/^{238}U$ and $^{207}Pb/^{235}U$ results plotted on a Concordia diagram are relatively consistent, yielding a Concordia age of 209.0 ± 1.4 Ma, interpreted as the Late Triassic crystallization age of the syenogranite (Fig. 6, Tab. 1). This age is in agreement with previous age at 207 ± 1 Ma (Liu et al., 2012; Fig. 2). Th/U ratios of Sample WTF13 range from 0.38 to 1.50. Nineteen analyses of $^{206}Pb/^{238}U$ and $^{207}Pb/^{235}U$ results show a Concordia age of 208.8 ± 1.8 Ma (Fig. 6, Tab. 1). It corresponds to the Late Triassic emplacement age of the diorite, older than a previous age at 191 ± 1 Ma (Liu et al., 2012; Fig. 2). The ages of the syenogranite and diorite are the same within errors.

4.2 Major and trace elements analyses

Analyses of whole-rock major and trace elements were carried out at the IGGCAS. Major elements were analysed by X-ray spectrometry. Analytical precision is estimated at 1–5% for major elements. Trace elements were determined by inductively coupled plasma mass spectrometry (ICP-MS). The major- and trace-element data are documented in Tab. 2. The

syenogranite samples have high SiO_2 contents ranging from 75.05 to 77.01 wt %. All samples are relatively high in Al_2O_3 (12.44–13.34 wt %), Na_2O (3.51– 4.06 wt %) and total alkalis (K_2O+ Na_2O, 8.42–8.91 wt %), with Na_2O/K_2O ratios of 0.71–0.84. They are low in P_2O_5 (0.02–0.04 wt %) and TiO_2 (0.12–0.19 wt %) abundances, and have Mg number # of 6.76–17.73. In the total alkali versus silica diagram (Fig. 7a), all samples plot in granite field. The diorite displays a SiO_2 abundance of 51.88–56.31 wt %. It is characterized by a high Al_2O_3 content (15.78–19.66 wt %), a wide K_2O range of 1.46–3.50 wt % and total alkalis (K_2O+ Na_2O, 6.68–8.16 wt %), with Na_2O/K_2O ratios of 1.33–2.97. They have relatively high $Fe_2O_3^T$ (7.77–9.14 wt %) and low MgO (2.52–3.63 wt %) contents, with Mg # of 30.67–51.97. The samples plot in the monzodiorite and monzonite fields in the total alkali versus silica diagram (Fig. 7a). Both the syenogranite and the diorite are peraluminous (Fig. 7b) and can be categorized as high-K calc-alkaline series rocks (Fig. 7c).

The syenogranite and the diorite have total rare Earth element contents (∑REE) varying over 29.84–240.38 ppm, and 169.96–414.57 ppm, respectively, and both display right-dipping chondrite-normalized REE patterns (Fig. 8a). Their ∑LREE/∑HREE ratios are 5.92–15.17 and 6.28–10.25, respectively. The syenogranite displays $(La/Yb)_N$ and $(Gd/Yb)_N$ ratios of 3.21–15.81 and 0.74–1.26 with high negative Eu anomalies (Eu/Eu* = 0.16–0.54), whereas the diorite shows $(La/Yb)_N$ and $(Gd/Yb)_N$ ratios of 9.76–14.12 and 1.87–5.03 with low negative Eu anomalies (Eu/Eu* = 0.64–0.94) (Fig. 8a). In the primitive mantle-normalized variation diagrams (Fig. 8b), the syenogranite and the diorite samples are both enriched in large-ion lithophile elements (LILE) relative to high field strength elements (HFSE). Their REE and trace element patterns are similar to the contemporaneous Dushan batholith to its south (Ye et al., 2014, Fig. 1).

4.3 *In-situ* zircon Hf isotopes

Previously analyzed zircon grains for U-Pb isotopes were chosen for *In-situ* zircon Hf isotopic analyses. It was carried out in situ on a Neptune multi-collector ICP-MS equipped with a Geolas-193 laser ablation system at IGGCAS. Results for in situ Hf isotope analyses of zircons are shown in Fig. 9 and Tab. 3. Zircons from the syenogranite (WTF5) have variable Hf isotopic compositions, $^{176}Hf/^{177}Hf$ ratios between 0.282377015 and 0.282469207, εHf(t) values between –9.78 and –6.54, and two-stage depleted mantle Hf model (t_{DM2}) ages between 1840.9 and 1635.3 Ma. Zircons from the diorite (WTF13) have $^{176}Hf/^{177}Hf$ ratios between 0.282555378 and 0.282665470, a range of εHf(t) values varying from –3.42 to –0.01, and two-stage depleted mantle Hf model (t_{DM2}) ages between 1439.9 and 1205.6 Ma. Magmatic zircons from the Wangtufang pluton exhibit similar εHf(t) values from −13.69 to 3.94, and two-stage depleted mantle Hf model (t_{DM2}) ages from 1582 to 950 Ma in the contemporaneous plutons (Yang et al., 2012; Zhang et al., 2012; Ye et al., 2014; Xiong et al., 2017).

5. Anisotropy of magnetic susceptibility

Field and microscopic observations suggest that both planar and linear fabrics cannot be directly observed in the Wangtufang pluton. Magnetic fabrics can often record the fabric elements of anisotropic rocks where macro and microscopic features fail to do it (Archanjo et al., 1994; Bouchez and Gleizes, 1995; Bouchez et al., 1997). In order to assess the fabric elements, an AMS study has been carried out. Two hundred and four cores from 36 sites have been sampled for AMS measurements in the Wangtufang pluton, 20 in the syenogranite and 16 in the diorite. The measurements are realized in the Laboratory of Paleomagnetism and Chronology of IGGCAS. A total of 204 cores from 36 sampling sites were cut into cylindrical specimens of 2.2 cm in length and 2.5 cm in diameter. The anisotropy magnetic susceptibility and the bulk susceptibility were measured with a KLY4 susceptometer. The mean orientation of three principal axes of the AMS

ellipsoid ($K_1 \geq K_2 \geq K_3$), the shape parameter (T), and the anisotropy degree (P_J) were calculated by the ANISOFT package (Jelinek, 1981). The magnetic mineralogy was investigated to identify the magnetic susceptibility carriers by several methods, including: (1) Isothermal Remanent Magnetization (IRM); (2) thermomagnetic (K-T) curves, and (3) hysteresis loops.

5.1 Magnetic mineralogy

The histogram of mean magnetic susceptibility, $K_m = (K_1 + K_2 + K_3)/3$, displays a large range of values in 36 sites, from 90 to 95,900×10^{-6} SI (Fig. 10a and Tab. 4). In the diorite, all 16 sites exhibit K_m values higher than 7,000×10^{-6} SI (7,540 to 95,900×10^{-6} SI), demonstrating the predominance of ferromagnetic minerals. In the syenogranite, K_m mainly varies from about 90 to 15,400×10^{-6} SI, and 7 out of 20 sites show K_m values lower than 500×10^{-6} SI, implying that the paramagnetic minerals (biotite) may be the main carriers of the magnetic susceptibility (e.g., Tarling and Hrouda, 1993). In 13 out of 20 sites, K_m values are higher than 500×10^{-6} SI, suggesting the presence of ferromagnetic minerals. It seems that both paramagnetic and ferromagnetic minerals are the contributors to the magnetic fabrics in the syenogranite.

All hysteresis curves of six representative samples display nonlinear variations (Figs. 11a–11c). Sudden saturation of the isothermal magnetic remanence below 300 mT occurs in all samples (Figs. 11d–11f). Thermomagnetic measurements show a rapid drop of magnetic susceptibility at ~580°C (Figs. 11g–11i). All these results suggest that magnetite is likely an overwhelming contributor to the magnetic carriers in the Wangtufang pluton despite the presence of biotite. The ratios of hysteresis parameters Mr/Ms and Hcr/Hc display the mean grain size of the magnetite of the analyzed samples is within the pseudo-single domain (PSD) zone (Dunlop, 2002; Fig. 12), indicating that the principal axes of the magnetic susceptibility ellipsoid (K_1 and K_3 measured in

this study) correspond to the major morphological axes of minerals, representing magnetic lineation and the pole of magnetic foliation, respectively.

More than 92% of the sampled sites display an anisotropy degree (P_J) lower than 1.2 (Figs. 10b and 10c), concordant with the magmatic fabrics recognized by microscopic observations, and the remaining sites come from the diorite, implying that their higher P_J value may be due to the high concentration of magnetite (Cruden, et al., 1999). The shape parameter (T) mainly ranges between -0.551 and 0.829, showing a dominant oblate shape (~86%) for magnetic fabrics (Figs. 10c and 10d). Obvious correlations between P_J, T, and K_m is lacking, implying that AMS varies independently from the magnetic minerals (Borradaile and Henry, 1997; Figs. 10b–10d).

5.2 AMS results

The site-average orientation with corresponding 95% confidence level (α_{95max} and α_{95min}) was calculated for K_1 and K_3 axes of each site (Jelinek, 1978; Fig. 13). For a confidence level larger than 25°, the direction of the corresponding magnetic axis is considered as poorly defined, whereas it is considered as well-defined or reliable when lower than 25°. More than 78 % of the AMS sites are well defined for both K_1 and K_3. The magnetic fabrics were mapped throughout the Wangtufang pluton (Fig. 14).

At the map scale, the magnetic foliations in the diorite strike subparallel to the pluton boundary and dip inward at variable angles (Fig. 14a). The magnetic lineations are highly scattered with variable dips (Fig. 14b). This may be due to an overprint by the late-stage tectonomagmatism. Instead, in the syenogranite, both the magnetic foliations and lineations are highly grouped (Fig. 14a). Magnetic foliations, also parallel to the pluton boundary, display a concentric arrangement. The majority of specimen (14 out of 20 sites) show subhorizontal foliations with dip angles ranging from 3° to 40°. Specimens from six sites have moderately steep magnetic foliations (dip angles

ranging from 45° to 70°). These sites are almost near the contacts with the country rock and the diorite. The magnetic lineations are all horizontal to subhorizontal (mainly ~9° to 29°) and have nearly constant NE–SW plunges (Fig. 14b).

6. Gravity modeling

Gravity modeling has been long proved its efficiency to constrain the geometry and possible feeder zones of pluton (e.g., Vigneresse et al., 1990; Améglio and Vigneresse, 1999; Lin et al., 2013b). We carried out a gravity study to characterize the shape of the Wangtufang pluton at depth.

6.1 Residual Bouguer anomaly and 2D modeling

The short wavelengths of the gravity anomaly originate from upper crust (down to a few kilometers). The long wavelengths of the gravity anomaly, which reflect the deep structures, must be removed from the complete Bouguer anomaly to highlight the Wangtufang pluton related anomalies. Available Bouguer anomaly map (1: 200,000) in the Wangtufang pluton and its surrounding area was derived from the Chinese regional gravity survey. A regional lower-resolution (2′×2′) Bouguer grid acquired from the International Gravimetric Bureau database (Bonvalot et al., 2012). The long wavelengths of the gravity anomaly were extracted using a 200 km low-pass Butterworth filter from a lower-resolution (2′×2′) Bouguer grid after several attempts. The residual Bouguer anomaly map was obtained from the complete Bouguer anomaly by subtracting the filtered regional Bouguer anomaly related to the long wavelengths (Fig. 15a).

2D gravity modeling was also performed to characterize the geometry of the Wangtufang pluton. To build these models, several constraints have been taken into account, including (1) geological contacts, lithological units, and structural data from geological maps and our field observations; (2) geometrical constraints, derived from indirect analysis of gravity anomaly, and

(3) densities of geological units, determined by the laboratory measurements. The residual gravity anomaly has been modelled along three profiles across the center of the pluton (Fig. 15b).

6.2 Results

In the residual Bouguer gravity anomaly map, the Wangtufang pluton displays a NE–SW trending elongated negative anomaly with a highest value in its center (Fig. 15a). The negative anomalies decrease, even change into positive anomalies outwards. Particularly, the diorite shows a less negative anomaly in its northwest and a higher positive anomaly in its southeast, suggesting its thin thickness. The Wangtufang pluton becomes thinner outwards, presenting an overall funnel-shaped geometry. The country rocks display high positive anomalies in its east. To the southwest, the country rocks show a high negative anomaly, indicating the possible continuity of the pluton underlain the country rocks. The highest negative anomaly is located in its northwest due to a large area of Archaean migmatitic granite. Three 2D modeling profiles image the detailed geometry of the two major intrusions (Fig. 15b), revealing (1) a thin thickness of the diorite that overlies the syenogranite; (2) a maximal thickness of about 4 km in the center of the syenogranite which progressively decreases outwards; (3) a slightly NE–SW trending elongated subsurface shape of the syenogranite with inward dipping sidewalls.

7. Discussion

7.1 Magma sources of the Wangtufang pluton

Both high SiO_2 syenogranite and relatively low SiO_2 diorite are characterized by low MgO, enrichment in LREE and LILE, and depletion in HREE and HFSE, with negative Eu anomalies (Figs. 7 and 8), suggesting that they mainly derived from partial melting of ancient lower crust. However, their in-situ zircon two-stage depleted mantle Hf model ages (t_{DM2}) are both Proterozoic, ranging from ~1.840 to 1.635 Ga and ~1.439 to 1.205 Ga, respectively (Fig. 9). Considering that

313 the Wangtufang pluton intrudes into Archaean gneiss and migmatitic granite (＞2.5 Ga), the
314 sources should be derived from the partial melting of Archean TTG in the lower crust with a
315 contribution from a depleted mantle source. The $\varepsilon_{Hf}(t)$ values for the syenogranite range from –
316 9.78 to –6.54 and those of the diorite from –3.42 to –0.01 (Fig. 9). Although the diorite was mainly
317 derived from melting of ancient lower crust, $\varepsilon_{Hf}(t)$ values of the diorite are much higher than
318 normal crustal melting (Fig. 9), requiring some input of depleted asthenospheric mantle
319 components. The $\varepsilon_{Hf}(t)$ values of the syenogranite are higher than those of the Archean lower crust
320 (-28 ~ -13; Jiang et al., 2013). It suggests that the syenogranite has a contribution from an enriched
321 subcontinental lithospheric mantle. Therefore, the Wangtufang pluton was mainly derived from
322 partial melting of the ancient lower crust of the NCC with some involvements of enriched
323 subcontinental lithospheric mantle and depleted asthenospheric mantle components. Coeval with
324 the Wangtufang pluton, Late Triassic silica-undersaturated syenites in the alkaline complexes in
325 the northern NCC were derived from partial melting of an enriched lithospheric mantle, coupled
326 with crustal assimilation and crystal fractionation in an intracontinental extensional setting (i.e.,
327 rift; Yang et al., 2012). Its similarity with the contemporaneous alkaline complexes may indicate
328 an asthenosphere–lithospheric mantle interaction in the northern NCC during the Late Triassic
329 (Yang et al., 2012; Zhang et al., 2012). Briefly, the Wangtufang pluton was derived from the
330 mixing of magmas from asthenospheric upwelling-induced melting of subcontinental lithospheric
331 mantle and ancient lower crust during an intracontinental extensional setting.

332 **7.2 Emplacement model**

333 Geochronology data suggest that both the syenogranite and the diorite were emplaced in
334 the Late Triassic (both at ~209 Ma; Fig. 6). Concerning the fabric pattern of the diorite, magnetic
335 foliations show variable dip angles and scattered magnetic lineations, and this may be due to the

later intrusion of the syenogranite (Fig. 14). The border-parallel magnetic foliations are usually considered as a consequence of magma inflation during the intrusion. Gravity modeling reveals thin remnants of diorite, which are close to the roof of the syenogranite (Fig. 15). Furthermore, field observations indicate that numerous syenogranite dykes intruded into the diorite with sharp contact and dismembered the diorite after its fully crystallization (Fig. 4). As the fabric pattern seems to be modified, it is difficult to retrace the emplacement process of the diorite, therefore, we shall focus on the emplacement of the syenogranite.

In the syenogranite, the current exposure is close to the roof of the pluton due to the covering of the diorite remnants (Fig. 15). The mostly subhorizontal magnetic foliations, roughly parallel to the contact, develop near the roof (Fig. 14a). Bouguer gravity anomaly reveals a NE-SW trending elongated subsurface shape with an overall funnel-shaped geometry, an unflat bottom, and moderate- to high- inward dipping sidewalls (Fig. 15). The root of the syenogranite as a feeder zone is located in its center. Thus, it might be estimated as a lopolith-like intrusion (Fig. 16). Considering the lack of significant emplacement-related ductile deformation in the country rocks, the syenogranite with a concentric fabric pattern could emplace by the inflation of the magma from its central feeder zone and the pluton is built up by floor depression (Fig. 16). The subhorizontal magnetic fabrics could have developed by magmatic flow subparallel to a roof, represented by the floor of the diorite (e.g., McNulty et al., 2000). A dominant gentle magnetic fabric could be formed by flattening of magma mush against its roof, driven by later magma pulses (McNulty et al., 2000). The arrivals of later magma batches resulted in downward inflation of magma chamber against the roof. Floor depression occurred and created space for the pluton building (Fig. 16). Close to the pluton, the country rocks were pushed aside and it resulted in the border-parallel foliations in the surrounding gneiss (Fig. 2). We suggest that the diorite made a

first intrusion, probably with a thin thickness, and then the syenogranite intruded and possibly dismembered the former with a series of dykes after the diorite had fully crystallized (Fig. 16).

7.3 Relationships between the pluton emplacement and regional tectonics

The microstructures observed in the Wangtufang pluton are typical of magmatic or sub magmatic fabrics that developed during, or just after, the full crystallization of the magma. However, the lack of significant emplacement-related ductile deformation in both the pluton and its country rocks does not preclude that a regional tectonic event, dominated by brittle deformation occurred during the Wangtufang pluton emplacement. The syenogranite intruded the diorite after its full crystallization as shown by the dyke swarm containing diorite xenoliths (Fig. 4b). All the syenogranitic dykes are steeply dipping and striking NW–SE. We interpret these syenogranite dykes as tension gashes developed in the brittle upper crust, and controlled by a NE–SW stretching. This view implies a possible NE–SW trending regional extension (Fig. 16).

Moreover, the plutons shape and internal fabric can record some increments of the regional strain to which the magma was subjected (e.g., Paterson et al., 1998; Sant'Ovaia et al., 2000). Because mineral fabrics are easily reset, they reflect only the last strain increment developed in soft material such as magmatic rocks before their full crystallization. Furthermore, without any regional strain or pre-existing structural control, the magmatic lineation that reflects the magma flow within the pluton would have variable orientations and plunges (e.g., Paterson, 1989; Liu et al., 2018). Thus, we argue that the syenogranite, presenting a general NE–SW magnetic lineation, may have recorded a NE–SW trending regional extension (Fig. 16). Meanwhile, the pluton growth could have been guided by the NE–SW trending regional tectonic regime, suggested by a NE–SW trending elongated subsurface shape of the pluton (Fig. 15a).

Geochemical data suggest that the Wangtufang pluton was derived from the partial melting of Archaean TTG in the lower crust with a contribution from a depleted mantle source. This feature is consistent with the geochemical characteristics of the E–W trending alkaline intrusive complexes along the northern NCC (Zhang et al., 2012; Fig. 17). Especially, the silica-undersaturated syenites comply with a Late Triassic intracontinental extensional setting after the final formation of the Central Asian Orogenic Belt (Yang et al., 2012; Fig. 17). Besides, a NE–SW trending regional extension in the northern NCC has been documented in the Sonid Zuoqi MCC in the vicinity of the Solonker zone (Davis et al., 2004; Fig. 17). The $^{40}Ar/^{39}Ar$ ages of muscovite in the detachment fault were 224~208 Ma. Detrital zircon dating and sedimentological studies of these basin remnants showed a fining and deepening upward depositional system as well as abundant volcaniclastic rocks from the conformable Upper Triassic to Lower Jurassic strata, suggesting a Late Triassic extensional tectonic setting (Davis et al., 2009; Meng et al., 2014; Fig. 1). The emplacement of the Wangtufang pluton provides new structural constraints on the Late Triassic NE–SW trending extensional setting in the northern NCC.

8. Conclusions

A multidisciplinary study, including geochronology and geochemistry, field and microscopic observations, anisotropy of magnetic susceptibility (AMS), and gravity investigation, has been carried out to characterize the emplacement mode and tectonic setting of the Late Triassic Wangtufang pluton. These results reveal that: (1) both the syenogranite and the diorite in the Wangtufang pluton are derived from the partial melting of the lower crust with a contribution from a depleted mantle source; (2) the diorite, represented just by thin remnants, was intruded and dismembered by the later syenogranite intrusion coeval with a NW–SE trending dyke swarm after the diorite full crystallization; (3) the syenogranite, a lopolith-like intrusion, emplaced by the

inflation of magma batches from a conduit in its center, and the emplacement space was mainly created by floor depression for the pluton building; (4) if the consistently NW–SE striking dykes may be considered as tension gashes, the Wangtufang pluton emplaced in a NE–SW trending regionally extensional tectonic setting, providing more reliable arguments to the Late Triassic intracontinental extensional setting already suggested in the northern NCC.

Acknowledgements

This work has been financially supported by the National Key R&D Program of China (2016YFC0600102 and 2016YFC0600401) and the NSFC (91855212, 91755205, and 41472193). Prof. Sanzhong Li and two anonymous reviewers together with the editors are very much thanked for their constructive comments and suggestions, which lead to a great improvement of our manuscript.

References

Améglio, L., Vigneresse, J.L., 1999. Geophysical imaging of the shape of granitic intrusions at depth: a review. Geological Society, London, Special Publications 168 (1), 39–54. https://doi.org/10.1144/GSL.SP.1999.168.01.04

Archanjo, C.J., Launeau, P., Bouchez, J.L., 1994. Magnetic fabrics vs. magnetite and biotite shape fabrics of the magnetite-bearing granite pluton of Gameleiras (Northeast Brazil). Physics of the Earth and Planetary Interiors 89 (1–2), 63–75. https://doi.org/10.1016/0031- 9201(94)02997-P

Blanquat, M.D.S., Horsman, E., Habert, G., Morgan, S., Vanderhaeghe, O., Law, R., Tikoff, B., 2011. Multiscale magmatic cyclicity, duration of pluton construction, and the paradoxical relationship between tectonism and plutonism in continental arcs. Tectonophysics 500 (1–4), 20–33. https://doi.org/10.1016/j.tecto.2009.12.009

427 Bonvalot, S., Balmino, G., Briais, A., Kuhn, M., Peyrefitte, A., Vales, N., Biancale, R., et al.,
428 2012. World gravity map. (1:50000000 map), BGI-CGMWCNES-IRD, Paris.
429 Borradaile, G.J., Henry, B., 1997. Tectonic applications of magnetic susceptibility and its
430 anisotropy. Earth-Science Reviews 42 (1–2), 49–93. https://doi.org/10.1016/S0012-
431 8252(96)00044-X
432 Bouchez, J.L., Gleizes, G., 1995. Two-stage deformation of the Mount-Louis-Andorra granite
433 pluton (Variscan Pyrenees) inferred from magnetic susceptibility anisotropy. Journal of
434 the Geological Society 152 (4), 669–679. https://doi.org/10.1144/gsjgs.152.4.0669
435 Bouchez, J.L., Hutton, D., Stephens, W.E., 1997. Granite is Never Isotropic: An Introduction to
436 AMS Studies of Granitic Rocks. Granite: From Segregation of Melt to Emplacement
437 Fabrics (pp. 95–112). Paris: Springer Science and Business Media.
438 https://doi.org/10.1007/978-94-017-1717-5_6
439 Castro, A., 1987. On granitoid emplacement and related structures: A review. Geologische
440 Rundschau 76 (1), 101–124. https://doi:10.1007/BF01820576
441 Cruden, A. R., Tobisch, O. T., Launeau, P., 1999. Magnetic fabric evidence for conduit-fed
442 emplacement of a tabular intrusion: Dinkey Creek Pluton, central Sierra Nevada
443 batholith, California. Journal of Geophysical Research: Solid Earth 104 (B5), 10511–
444 10530. https://doi:10.1029/1998jb900093
445 Davis, G.A., Meng, J.F., Cao, W.R., 2009. Triassic and Jurassic tectonics in the eastern Yanshan
446 belt, North China: insights from the controversial Dengzhangzi Formation and its
447 neighboring units. Earth Science Frontiers 16 (3), 69–86. https://doi.org/10.1016/S1872-
448 5791(08)60090-1
449 Davis, G.A., Xu, B., Zheng, Y.D., Zhang, W.J., 2004, Indosinian extension in the Solonker

suture zone: the Sonid Zuoqi metamorphiccore complex, Inner Mongolia, China. Earth Science Frontiers 11 (3), 135–144. https://doi.org/ 10.1007/BF02873097

Davis, G.A., Zheng, Y.D., Wang, C., 2001. Mesozoic tectonic evolution of the Yanshan fold and thrust belt, with emphasis on Hebei and Liaoning provinces, northern China. In: Hendrix, M.S., Davis, G.A. (Eds.), Paleozoic and Mesozoic tectonic evolution of central Asia: From continental assembly to intracontinental deformation, Boulder, Colorado. Geological Society of America Memoir 194, 171–197.

Daoudene, Y., Ruffet, G., Cocherie, A., Ledru, P., Gapais, D., 2013. Timing of exhumation of the Ereendavaa metamorphic core complex (north-eastern Mongolia) U–Pb and $^{40}Ar/^{39}Ar$ constraints. Journal of Asian Earth Sciences 62, 98–116. https://doi.org/10.1016/j.jseaes.2011.04.009

De Saint Blanquat, M., Horsman, E., Habert, G., Morgan, S., Vanderhaeghe, O., Law, R., Tikoff, B., 2011. Multiscale magmatic cyclicity, duration of pluton construction, and the paradoxical relationship between tectonism and plutonism in continental arcs. Tectonophysics 500 (1–4), 20–33. https://doi.org/10.1016/j.tecto.2009.12.009

Dong, S., Zhang, Y., Zhang, F., Cui, J., Chen, X., Zhang, S., Miao, L., Li, J., Shi, W., Li, Z., Huang, S., Li, H., 2015. Late Jurassic–Early Cretaceous continental convergence and intracontinental orogenesis in East Asia: a synthesis of the Yanshan revolution. Journal of Asian Earth Sciences 114, 750–770. https://doi.org/10.1016/j.jseaes.2015.08.011

Dunlop, D.J., 2002. Theory and application of the day plot (Mrs/Ms versus Hcr/Hc) 1. Theoretical curves and tests using titanomagnetite data. Journal of Geophysical Research 107 (B3), 2056. https://doi.org/10.1029/2001JB000487

Faure, M., Lin, W., Chen, Y., 2012. Is the Jurassic (Yanshanian) intraplate tectonics of North

China due to westward indentation of the NCC? Terra Nova 24 (6), 456–466. https://doi.org/10.1111/ter.12002

Faure, M., Trap, P., Lin, W., Monié, P., Bruguier, O., 2007. Polyorogenic evolution of the Paleoproterozoic Trans-North China Belt, new insights from the in Lüliangshan-Hengshan-Wutaishan and Fuping massifs. Episodes Journal of International Geoscience, Seoul National University 30 (2), 95–106.

Hacker, B.R., Ratschbacher, L., Webb, L., McWilliams, M.O., Ireland, T., Calvert, A., Dong, S., Wenk, H., Chateigner, D., 2000. Exhumation of ultrahigh-pressure continental crust in east central China: Late Triassic-Early Jurassic tectonic unroofing. Journal of Geophysical Research: Solid Earth 105 (B6), 13339–13364. https://doi.org/10.1029/2000JB900039

Jelinek, V., 1978. Statistical processing of anisotropy of magnetic susceptibility measured on groups of specimens. Studia Geophysica et Geodaetica 22 (1), 50–62. https://doi.org/10.1007/BF01613632

Jelinek, V., 1981. Characterization of the magnetic fabric of rocks. Tectonophysics 79 (3–4), 63–67. https://doi.org/10.1016/0040-1951(81)90110-4

Jiang, N., Guo, J., Chang, G., 2013. Nature and evolution of the lower crust in the eastern North China craton: A review. Earth-Science Reviews 122, 1-9.

Li, C., Zhang, C., Cope, T. D., Lin, Y., 2016. Out-of-sequence thrusting in polycyclic thrust belts: an example from the Mesozoic Yanshan belt, North China Craton. Tectonics 35, 2082–2116. https://doi.org/10.1002/2016TC004187

Li, S.Z., Kusky, T.M., Zhao, G.C., Liu, X.C., Wang, L., Kopp, H., Hoernle, K., Zhang, G.W., Dai, L.M., 2011. Thermochronological constraints on Two-stage extrusion of HP/UHP

terranes in the Dabie-Sulu orogen, east-central China. Tectonophysics 504, 25-42.

Li, S.Z., Kusky, T.M., Zhao, G.C., Liu, X.C., Zhang, G.W., Kopp, H., Wang, L., 2010. Two-stage Triassic exhumation of HP-UHP terranes in the Dabie orogen of China: constraints from structural geology. Tectonophysics 490, 267-293.

Li, S.Z., Jahn, B.M., Zhao, S.J., Dai, L.M., Li, X.Y., Suo, Y.H., Guo, L.L., Wang, Y.M., Liu, X.C., Lan, H.Y., Zhou, Z.Z., Zheng, Q.L., Wang, P.C., 2017. Triassic southeastward subduction of North China Block to South China Block: insights from new geological, geophysical and geochemical data. Earth-Science Reviews 166, 270-285.

Li, S.Z., Zhao, G.C., 2007. SHRIMP U-Pb zircon geochronology of the Liaoji Granitoids: constraints on the Paleoproterozoic Jiao-Liao-Ji belt in the eastern block of the North China craton. Precambrian Research 158 (1-2), 1-16.

Li, S.Z., Zhao, G.C., Dai, L.M., Liu, X., Zhou, L.H., Santosh, M., Suo, Y.H., 2012. Mesozoic Basins in eastern China and their Bearings on the deconstruction of the North China Craton. Journal of Asian Earth Sciences 47, 64-79.

Li, S.Z., Zhao, G.C., Santosh, M., Liu, X., Dai, L.M., Suo, Y.H., Tam, P.Y., Song, M.C., Wang, P.C., 2012. Paleoproterozoic structural evolution of the southern segment of the Jiao-Liao-Ji Belt, North China Craton. Precambrian Research 200-203, 59-73.

Li, S.Z., Zhao, S.J., Liu, X., Cao, H.H., Yu, S., Li, X.Y., Somerville, I., Yu, S.Y., Suo, Y.H., 2018. Closure of the Proto-Tethys Ocean and Early Paleozoic amalgamation of microcontinental blocks in East Asia. Earth-Science Reviews 186, 37-75.

Lin, W., Charles, N., Chen, K., Chen, Y., Faure, M., Wu, L., Wang, F., 2013b. Late Mesozoic compressional to extensional tectonics in theYiwulüshan massif, NE China and its bearing on the evolution of the Yinshan–Yanshan orogenic belt part II: Anisotropy of

519 magnetic susceptibility and gravity modeling. Gondwana Research 23 (1) 78–94.
520 https://doi.org/10.1016/j.gr.2012.02.012
521 Lin, W., Faure, M., Chen, Y., Ji, W. B., Wang, F., Wu, L., Charles, N., 2013a. Late Mesozoic
522 compressional to extensional tectonics in the Yiwulüshan massif, NE China and its
523 bearing on the evolution of the Yinshan–Yanshan orogenic belt part I: Structural analyses
524 and geochronological constraints. Gondwana Research 23 (1), 54–77.
525 https://doi.org/10.1016/j.gr.2012.02.013
526 Lin, W., Wei, W., 2018. Late Mesozoic extensional tectonics in the North China Craton and its
527 adjacent regions: A review and synthesis. International Geology Review.
528 https://doi.org/10.1080/00206814.2018.1477073
529 Liu, H., Martelet, G., Wang, B., Erdmann, S., Chen, Y., Faure, M., Huang, F., Scaillet, B., le-
530 Breton, N., Shu, L., Wang, R., Zhu, J., 2018. Incremental emplacement of the Late
531 Jurassic midcrustal, lopolith-like Qitianling pluton, South China, revealed by AMS and
532 Bouguer gravity data. Journal of Geophysical Research: Solid Earth 123.
533 https://doi.org/10.1029/2018JB015761
534 Liu, J., Zhao, Y., Liu, X., Wang, Y., Liu, X., 2012. Rapid exhumation of basement rocks along
535 the northern margin of the North China craton in the early Jurassic: Evidence from the
536 Xiabancheng Basin, Yanshan Tectonic Belt. Basin Research 24 (5), 544–558.
537 https://doi.org/10.1111/j.1365-2117.2011.00538.x
538 Ma, Y.S., Zeng, Q.L., Song, B., Du, J.J., Yang, F.Q., Zhao, Y., 2007. SHRIMP U–Pb dating of
539 zircon from Panshan granitoid pluton in Yanshan orogenic belt and its tectonic
540 implications. Acta Petrologica Sinica 23, 547–556 (in Chinese with English abstract).
541 Mattauer, M., Matte, P., Malavieille, J., Tapponnier, P., Maluski, H., Qin, X.Z., Lu, Y.L., Tang,

Y.Q., 1985. Tectonics of the Qinling belt: build-up and evolution of eastern Asia. Nature 317 (6037), 496–500. https://doi.org/10.1038/317496a0

McNulty, B.A., Tobisch, O.T., Cruden, A.R., Gilder, S., 2000. Multistage emplacement of the mount givens pluton, central Sierra Nevada batholith, California. Geological Society of America Bulletin 112 (1), 119–135. https://doi.org/10.1130/0016-7606(2000)1122.3.CO;2

Meng, Q.R., Wei, H.H., Wu, G.L., Duan, L., 2014. Early Mesozoic tectonic settings of the northern North China Craton. Tectonophysics 611 (1), 155–166. https://doi.org/10.1016/j.tecto.2013.11.015

Meng, Q.R., Zhang, G.W., 1999. Timing of collision of the North and South China blocks: controversy and reconciliation. Geology 27 (2), 123–126. https://doi.org/10.1130/0091-7613(1999)027<0123:TOCOTN>2.3.CO;2

Paterson, S.R., Fowler, T.K., Schmidt, K.L., Yoshinobu, A.S., Yuan, E.S., Miller, R.B., 1998. Interpreting magmatic fabric patterns in plutons. Lithos 44 (1–2), 53–82. https://doi.org/10.1016/s0024-4937(98)00022-x

Paterson, S.R., Vernon, R.H., Tobisch, O.T., 1989. A review of criteria for the identification of magmatic and tectonic foliations in granitoids. Journal of Structural Geology 11 (3), 349–363.

Sant'Ovaia, H., Bouchez, J.L., Noronha, F., Leblanc, D., Vigneresse, J.L., 2000. Composite-laccolith emplacement of the post-tectonic Vila Pouca de Aguiar granite pluton (northern Portugal): a combined AMS and gravity study. Transactions of the Royal Society of Edinburgh: Earth Sciences 91 (1–2), 123–137. https://doi.org/10.1017/s026359330000732x

565 Tarling, D.H., Hrouda, F., 1993. Magnetic Anisotropy of Rocks. London, U. K.: Chapman and
566 Hall.
567 Vigneresse, J.L., 1990. Use and misuse of geophysical data to determine the shape at depth of
568 granitic intrusions. Geological Journal 25 (3–4), 249–260.
569 https://doi.org/10.1002/gj.3350250308
570 Wang, Y., Zhou, L., Zhao, L., 2013. Cratonic reactivation and orogeny: an example from the
571 northern margin of the North China Craton. Gondwana Research 24 (3–4), 1203–1222.
572 https://doi.org/10.1016/j.gr.2013.02.011
573 Windley, B.F., Alexeiev, D., Xiao, W., Kröner, A., Badarch, G., 2007. Tectonic models for
574 accretion of the Central Asian Orogenic Belt. Journal of the Geological Society 164 (1),
575 31–47. https://doi.org/10.1144/0016-76492006-022
576 Xiao, W., Windley, B.F., Sun, S., Li, J., Huang, B., Han, C., Yuan, C., Sun, M., Chen, H., 2015.
577 A tale of amalgamation of three Permo-Triassic collage systems in Central Asia:
578 oroclines, sutures, and terminal accretion. Annual Review of Earth and Planetary
579 Sciences 43 (1), 477–501. https://doi.org/10.1146/annurev-earth-060614-105254
580 Xiong, L., Wei, J., Shi, W., Fu, L., Li, H., Zhou, H., Chen, M., 2017. Geochronology, petrology
581 and geochemistry of the Mesozoic Dashizhu granites and lamprophyre dykes in eastern
582 Hebei – western Liaoning: implications for lithospheric evolution beneath the North
583 China Craton. Geological Magazine 1–24. https://doi.org/ 10.1017/S0016756817000437
584 Xu, B., Charvet, J., Chen, Y., Zhao, P., Shi, G., 2013. Middle Paleozoic convergent orogenic
585 belts in western Inner Mongolia (China): framework, kinematics, geochronology and
586 implications for tectonic evolution of the Central Asian Orogenic Belt. Gondwana
587 Research 23 (4), 1342–1364. https://doi.org/10.1016/j.gr.2012.05.015

588 Xu, Z., Lu, Y., Tang, Y., Mattauer, M., Matte, P., Malavieille, J., Tapponnier, P., Maluski, H.,
589 1986. Deformation characteristics and Tectonic evolution of the eastern Qinling orogenic
590 belt. Acta Geologica Sinica 60 (3), 23–35. https://doi.org/10.1111/j.1755-
591 6724.1986.mp60003003.x
592 Yang, J.H., Sun, J.F., Zhang, M., Wu, F.Y., Wilde, S.A., 2012. Petrogenesis of silica-saturated
593 and silica-undersaturated syenites in the northern North China Craton related to post-
594 collisional and intraplate extension. Chemical Geology 328 (11), 149–167.
595 https://doi.org/10.1016/j.chemgeo.2011.09.011
596 Ye, H., Zhang, S.H., Zhao, Y., Wu, F., 2014. Petrogenesis and emplacement deformation of the
597 Late Triassic Dushan composite pluton in the Yanshan fold and thrust belt: Implications
598 for the tectonic settings of the northern margin of the North China Craton during the
599 Early Mesozoic (in Chinese with English abstract). Earth Science frontiers 21 (4), 275–
600 292.
601 Zhang, S.H., Zhao, Y., Davis, G.A., Ye, H., Wu, F., 2014. Temporal and spatial variations of
602 Mesozoic magmatism and deformation in the North China Craton: implications for
603 lithospheric thinning and decratonization. Earth-Science Reviews 131 (4), 49–87.
604 https://doi.org/10.1016/j.earscirev.2013.12.004
605 Zhang, S.H., Zhao, Y., Ye, H., Hou, K.J., Li, C.F., 2012. Early Mesozoic alkaline complexes in
606 the northern North China Craton: implications for cratonic lithospheric destruction.
607 Lithos 155, 1–18. https://doi.org/10.1016/j.lithos.2012.08.009
608 Zhao, G., Wilde, S.A., Cawood, P.A., Sun, M., 2001. Archean blocks and their boundaries in the
609 North China Craton: lithological, geochemical, structural and P–T, path constraints and
610 tectonic evolution. Precambrian Research 107 (1) 45–73. https://doi.org/10.1016/S0301-

9268(00)00154-6

Zhao, P., Chen, Y., Xu, B., Faure, M., Shi, G., Choulet, F., 2013. Did the Paleo-Asian Ocean between NCC and Mongolia Block exist during the late Paleozoic? first paleomagnetic evidence from central-eastern Inner Mongolia, China. Journal of Geophysical Research: Solid Earth 118 (5), 1873–1894. https://doi.org/10.1002/jgrb.50198

Zhao, P., Faure, M., Chen, Y., Shi, G., Xu, B., 2015. A new Triassic shortening-extrusion tectonic model for Central-Eastern Asia: Structural, geochronological and paleomagnetic investigations in the Xilamulun Fault (North China). Earth and Planetary Science Letters 426, 46–57. https://doi.org/10.1016/j.epsl.2015.06.011

Zhao, Y., 1990. The Mesozoic orogenesis and tectonic evolution of the Yanshan area. Geological Review 36 (1), 1–13 (in Chinese with English abstract).Zorin, Y.A., 1999. Geodynamics of the western part of the Mongolia–Okhotsk collisional belt, Trans-Baikal region (Russia) and Mongolia. Tectonophysics 306 (1), 33–56. https://doi.org/10.1016/S0040-1951(99)00042-6

Figure Captions

Fig. 1. Simplified geological map of the Yanshan fold and thrust belt and location of the Wangtufang pluton. CFSZ: Chicheng-Fengning ductile shear zone, FLSZ: Fengning-Longhua, ductile shear zone, DNSZ: Damiao-Niangniangmiao ductile shear zone, UF: Unnamed fault, JXT: Jixian thrust, MLYA: Malanyu anticline, XBCB: Xiabancheng basin, NDB: Niuying-Dengzhangzi basin, WTF: Wangtufang pluton.

Fig. 2. Geological map and cross-sections in the Wangtufang pluton and its adjacent area. Numbers in circles and stereonet show the locations and attitudes of the measured dykes, respectively. U–Pb zircon data from Liu et al. (2012). See Fig. 1 for location.

Fig. 3. Field photographs of the Wangtufang pluton and its country rocks. (a) Syenogranite in the south of the Wangtufang pluton. (b) Diorite in the north of the Wangtufang pluton. (c) Archaean gneiss in the south of the Wangtufang pluton. (d) NW–SE trending lineation in Archaean gneiss. (e) Sigmoidal K-feldspar porphyroclast in Archaean gneiss, indicating a top-to-the-SE sense of shearing. (f) Migmatitic granite in the north of the Wangtufang pluton.

Fig. 4. Field photographs of the dykes and xenoliths in the Wangtufang pluton. (a) Syenogranitic dykes near the contact between the syenogranite and the diorite. (b) Dioritic xenoliths in the syenogranitic dykes. (c) Syenogranitic dykes near the northeastern border of the Wangtufang pluton. (d) Dioritic xenolith in the syenogranite.

Fig. 5. Microstructures of typical investigated samples in the Wangtufang pluton. (a) Distribution map of the different types of microstructures. (b) and (c) Magmatic microstructures in the syenogranite and the diorite, respectively. (d) and (e) Submagmatic microstructures in the syenogranite and the diorite, respectively.

Fig. 6. Cathodoluminescence (CL) images and U-Pb diagrams of Concordia age of representative zircons from collected samples. White solid ellipses are Secondary Ion Mass Spectrometer (SIMS) U-Pb analysis locations. White dashed circles are locations of LA-MC-ICPMS Hf analyses. Age and εHf(t) data are listed under individual zircons with ages ahead. MSWD: mean square of weighted deviates.

Fig. 7. Chemical analyses diagrams of major elements for the Wangtufang pluton. (a) SiO_2 vs. Na_2O+K_2O diagram. (b) SiO_2 vs. K_2O diagram. (c) Plot of A/CNK vs. ANK.

Fig. 8. Trace elements diagrams for the Wangtufang pluton. (a) Chondrite-normalized REE patterns. (b) Primitive mantle normalized element spider patterns.

Fig. 9. Diagram of $\varepsilon_{Hf}(t)$ vs. U-Pb ages Plot of all previously analyzed zircons for U-Pb isotopes in the Wangtufang pluton. Hf isotopic compositions of zircons from the contemporaneous plutons are from: Yang et al. (2012); Ye et al. (2014) and Xiong et al. (2017).

Fig. 10. AMS scalar parameters of the Wangtufang pluton. (a) Histogram of site mean magnetic susceptibility (K_m). (b) Anisotropy degree P_J value vs. Bulk magnetic susceptibility K_m. (c) Shape parameter T vs. Bulk magnetic susceptibility K_m. (d) Shape parameter T vs. anisotropy degree P_J value.

Fig. 11. Magnetic mineralogy investigations of representative specimens from the Wangtufang pluton. (a–c) hysteresis loops, (d–e) acquisition of isothermal remanent magnetization (IRM), and (g–i) thermomagnetic curves (K (T) curves).

Fig. 12. Day plot of hysteresis parameters. Mrs: saturation of magnetic remanence, Ms: saturation of induced magnetization, Hcr: coercivity of magnetic remanence, Hr: coercivity of the measured sample. SD: single domain, PSD: pseudo-singledomain, MD: multidomain.

Fig. 13. Equal-area projections (lower hemisphere) of AMS results for each sampling site. Confidence ellipses at 95% level are drawn around each average orientation direction.

Fig. 14. Mesoscopic and magnetic fabric patterns and orientation diagrams of K_3 and K_1. (a) Foliations. (b) Lineations.

Fig. 15. Gravity modeling. (a) Residual Bouguer gravity anomaly of the Wangtufang pluton and adjacent areas after subtraction of a 200 km wavelength regional trend from the complete Bouguer anomaly. Symbols and captions are the same as in Fig. 2. (b) 2D gravity modeling across the Wangtufang pluton. Note that the arrows show the possible feeder zones for the pluton.

Fig. 16. Block diagrams of emplacement mode of the Wangtufang pluton.

679 **Fig. 17.** Triassic tectonic framework of the NCC showing Late Triassic tectonic setting of the
680 northern NCC. XBCB: Xiabancheng basin, NDB: Niuying-Dengzhangzi basin, WTF:
681 Wangtufang pluton.

682 **Table 1.** SIMS zircon U-Pb data of the collected samples in the Wangtufang pluton.

683 **Table 2.** Major- and trace-element concentrations of the Wangtufang pluton.

684 **Table 3.** LA-ICP-MS in-situ Hf isotopic analyses of zircons for the Wangtufang pluton.

685 **Table 4.** The results of AMS measurements for the Wangtufang pluton. Lat: latitude, Long:
686 longitude, N: the number of cylinders measured in each site, K_m: mean magnetic susceptibility,
687 P_J and T: anisotropy degree and shape parameter, respectively, K_1 and K_3: magnetic lineation
688 and pole of magnetic foliation, respectively, Inc: inclination, and Dec: declination, α_{95max} and
689 α_{95min}: Jelinek's statistic confidence at 95% level (Jelinek, 1981) in degrees, respectively.